Comparison of ship detectors for polarimetric SAR imagery

David J Crisp and Thomas Keevers
Intelligence, Surveillance & Reconnaissance Division
Defence Science & Technology Organisation
PO Box 1500, Edinburgh, South Australia, 5111, Australia
Email: david.crisp@dsto.defence.gov.au

Abstract— **This paper examines the benefits of using fully polarimetric SAR imagery for ship detection. There are three related aspects to the work. First, RadarSat-2 quad-pol stripmap imagery is used to compare the performance of various ship detection algorithms/methods. The comparison is based on the use of ROC curves. Second, circular spotlight SAR imagery is used to examine how detector performance varies with the azimuth angle. Owing to the small number of available ship samples, this analysis has limitations. Third, again using the circular spotlight SAR imagery, the variation, with respect to azimuth angle, of the elements of the polarimetric covariance matrix of both the ship and the ocean are analysed. The results are as follows. Using the stripmap imagery, it is found that exploiting both polarimetry and spatial correlations greatly improves detection performance. Using the circular spotlight imagery, it is found that detection performance is variable with respect to azimuth angle and trends are hard to discern. Moreover, the performance of the Pauli double bounce detector is generally poor. It is conjectured that ship pitching motion degrades the polarimetric backscatter response in the circular spotlight imagery. Finally, the covariance matrix analysis confirms known trends for the ocean backscatter. The implication of these trends is that the polarimetric covariance matrix is sensitive to changes in azimuth angle and hence detectors based on them are also. The data indicate the extent to which this is the case.**

I. Introduction

Economical and effective maritime surveillance is a central concern for many commercial and government organisations. While high quality SAR images are widely available, the vast quantities of data available require efficient automated or semi-automated methods for analysis. Automated oceanic vessel detection is accomplished through statistical analysis of backscatter variations within an image. This paper considers several different detection algorithms/methods and applies them to different combinations polarimetric radar channels. Performance is compared using both ROC curve analysis and plots of the probability of detection at a fixed probability of false alarm.

Two different datasets are used in the analysis. The first is RadarSat-2 stripmap SAR imagery collected in the fine quad-pol mode. The second is circular spotlight SAR imagery collected using the DSTO Ingara multi-mode radar system. This later dataset allows the variation in detector statistics with azimuth angle to be studied. By definition the azimuth angle is the horizontal angular distance from a reference direction and so it defines the radar look direction with respect to the wind direction and the vessel heading. Both datasets have been calibrated so that the radar measurements represent backscatter coefficients.

The layout of the paper is as follows. The datasets, the method of performance evaluation, and the detection algorithms are described in the next three sections. Then in Section V the results for the stripmap SAR imagery are presented. These results clearly indicate the benefit of using fully polarimetric data. They also illustrate a significant additional benefit from exploiting the spatial correlations in the data. The circular spotlight SAR imagery results are presented in Section VI. However, the benefit of full polarimetry for this data set is not as good as expected. It appears the reason is distortions and mixing of the polarimetric information in the ship imagery caused by vessel motion while being imaged. Examples of sub-aperture imagery which illustrate this point are given. The penultimate section of the paper, Section VII, examines the variation of elements of the ocean polarimteric co-variance matrix with azimuth. The aim is to examine the sensitivity of the matrix (and hence detectors which use it) to changes in azimuth angle. Conclusions are given in the final section of the paper.

The following standard notation will be used. The cardinal linear polarisation channels are denoted by HH, HV, VH and VV. Here H denotes horizontal polarisation and V vertical. Further, the first symbol represents the transmit polarisation and the second the receive polarisation. The full scattering matrix is written as

$$[S] = \begin{bmatrix} S_{HH} & S_{HV} \\ S_{VH} & S_{VV} \end{bmatrix}.$$

II. Data sets

A. RadarSat-2 stripmap imagery

The RadarSat-2 stripmap imagery used in this paper was collected on 2 June 2009 in the ocean 25 kilometres south west of Marion Bay, South Australia. This area is exposed to the Southern Ocean swell which can be easily discerned in the imagery. The imagery contains two vessels - a 25 m long by 7.4 m wide vessel and a 11.6 m long vessel. Both vessels are made of metal and hence are radar bright. A light wind of about 5 m/s was blowing from the east and a low swell was present of about 1 m height from the south west.

978-1-4244-5222-4/10/$26.00 ©2010 CROWN

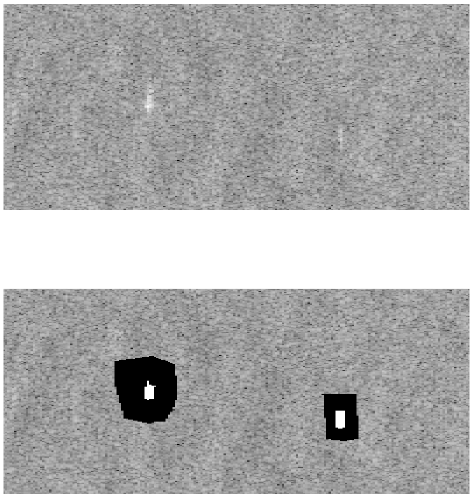

Fig. 1. Top - RadarSat-2 imagery. Bottom - manual ground-truthing of ship regions (white) with a mask (black) covering the uncertain regions. RADARSAT-2 Data and Product MacDonald, Dettwiler and Associates Ltd. (2009) All Rights Reserved.

RadarSat-2 operates at C-band. A fine quad-pol stripmap mode was used so that the full scattering matrix was measured. The resolution was 8 metres and the incidence angle was $40°$. The imagery used is shown in Figure 1.

B. Ingara circular spotlight imagery

The second data set contains circular spotlight imagery collected with DSTO's imaging radar system known as Ingara. The data was collected on 27 August 2004, near Port Lincoln, South Australia. The target of this imagery was a 22 m long prawn fishing vessel known as the Antica-S. The Antica-S is 7.4 m wide and has a metal hull and super-structure. She is equipped with trawl bars and a large crane. At the time of imaging she was at anchor in Spencer Gulf, South Australia. Her trawl bars deployed making a total width of approximately 25 metres. Both the trawl bars and the crane can be discerned at times in the imagery. An example of the imagery used together with manually marked ground truth is shown in Figure 2. As with the stripmap imagery, a guard area is placed around the ship to remove pixels which may contain both ship and ocean backscatter. Areas corrupted by thermal noise have also been masked out. These areas correspond to the edges of the azimuthal antenna footprint.

Ingara is fully polarimetric and the data was collected in all linear transmit-receive polarisation combinations (HH, HV, VH and VV) to measure the full scattering matrix. A recent description of the system may be found in [3] and the references therein cite earlier descriptions. During the trial Ingara was operated in a circular spotlight SAR mode. In this mode, the aircraft flies a circular orbit around the target with the radar beam pointed at the target. Data is collected continuously, allowing imagery to be formed at all $360°$ azimuth angles.

The subset of the data analysed here, was collected in one continuous run and is comprised of almost two complete

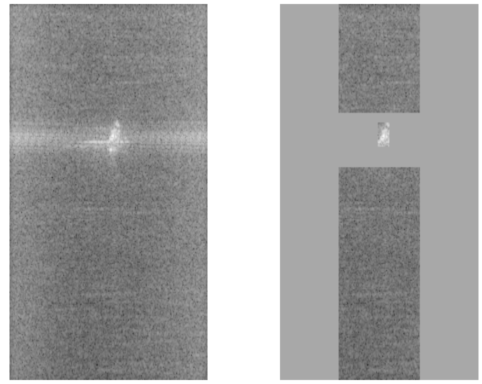

Fig. 2. Left - Ingara circular spotlight imagery. Right - manual masking of the ship and ocean regions. The mask is shown in mid-gray. The azimuthal direction is horizontal and range is vertical. Azimuthal smearing of the ship backscatter is clearly evident. Areas corrupted by thermal noise have also been masked out of each side of the imagery.

orbits. The incidence angle was nominally $50°$. The operating frequency was 10.1 GHz (X-band). The data was processed to a range and azimuth resolution of approximately 1 metre and was calibrated using standard techniques.

Equipment failure during the trial meant accurate wind and wave ground truth was not recorded. However, manual observations were made. The significant wave height was estimated to be 0.5 m which corresponds to a sea-state of 2. The gulf waters were sheltered from the Southern Ocean and no swell was present. The wind was estimated to be from NNE, at a strength of about 5 to 6 m/s. As is clear from the results presented later, the data corroborated these manual observations. Further, the manual ground-truth for vessel heading and the wind direction were assumed to be only approximate and hence were fine tuned using the data. In particular, they were matched to the known properties of the ocean co-variance matrix as discussed in the second to last section below.

III. PERFORMANCE EVALUATION

To quantify detector performance on the stripmap imagery, ROC curve analysis is used (see [1]). Through manual analysis of the stripmap SAR imagery, regions containing only ship pixels (white, see Figure 1 below) were isolated, and a small region around the ship in which pixel classification was uncertain (black) was also marked. For a given detector and threshold, probability of missed detections and false alarms are estimated empirically by counting the number of pixels which are classified incorrectly, divided by the total number of pixels in the ship and ocean samples, respectively. The complete ROC curve is generated by considering a sequence of detector thresholds. This simple estimator provides a useful method for characterising performance, however some limitations are discussed in [1]. Note also that it is more common for ROC curves to plot probability of detection rather than probability of missed detection, but the transformation between the two is straightforward.

Owing to a small number of ship samples, ROC curve analysis is not viable for the circular spotlight imagery. In its place, probabilities of detection at a fixed false alarm rate of 10^{-5} are used.

IV. Detection Algorithms

Below is a list of the detection algorithms we have considered. There are several other possibilities (see for instance Chapple *et al.* [2]) but the list has been limited here. A more comprehensive SAR imagery database than is currently available, with good ground-truth, is needed in order to contrast and compare subtle differences between similar detectors.

A. Single polarisation channel detectors

Of the single polarisation channels, it is well-known that both HH and HV produce good ship-ocean contrast depending on the incidence angles. The utility of the circular polarisation channels RR and LL (where R denotes right-circular and L denotes left circular) has also been discussed before [5]. Another channel of interest is the "cross-slant $45°$" polarisation channel [6]. This later channel consists of transmitting on a linear polarisation oriented at 45 degrees to the vertical and receiving on the orthogonal polarisation.

B. The "LRT" detector of Liu et al. [1]

Liu *et al.* [1]) assume the ocean and target backscatter follow a multi-variate Gaussian distribution of zero mean and develop a likelihood ratio test using the Neyman-Pearson criteria. This produces a decision variable

$$X^*(C_o^{-1} - C_s^{-1})X \qquad (1)$$

for each pixel, where

$$X = [S_{HH}, S_{HV}, S_{VH}, S_{VV}]^T$$

is the quad-polarimetric data for each pixel and, C_o and C_s are the covariance matrices (estimated from training data) for the ocean samples and ship samples, respectively, and $*$ denotes the complex conjugate transpose operator. It was found that typically the elements of the covariance matrix for the ship were much larger than those for the ocean so that the decision variable could be approximated by

$$X^* C_o^{-1} X.$$

The same simplification is used here since it avoids problems with the limited number of available ship samples. The matrix C_o is estimated using all the surrounding ocean. Liu *et al.* used this detector to quantify the extent to which additional polarimetric data channels can aid in target detection. Being based on the assumption of Gaussian statistics, this detector is not optimal (since measured magnitude data shows heavier histogram tails). This detector will be used as a benchmark for the others. It should be noted that the same collection of ocean pixels are used to both estimate C_o and evaluate detector performance. Hence the results presented here are better than would be achieved in practice.

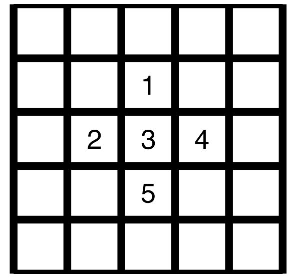

Fig. 3. The Significance Test Detector format.

C. Significance Test Detector of Chapple et al. [2]

The significance test detector of Chapple *et al.* [2] is modified here for use with fully polarimetric SAR data. The algorithm is similar to that of Liu *et al.* but also uses spatial correlation between bright pixels to enhance target detection. The decision variable is given by

$$Y^* C^{-1} Y$$

where Y is the vector

$$Y = [S_{HH}^{(1)}, S_{HV}^{(1)}, S_{VV}^{(1)}, \ldots, S_{HH}^{(5)}, S_{HV}^{(5)}, S_{VV}^{(5)}]^T$$

using the pixel grouping shown in Figure 3. As usual, C is the covariance matrix for the ocean samples and is estimated using all available ocean samples. Again, the same collection of ocean pixels are used to both estimate C and evaluate detector performance. The experiments here show that this detector provides a substantial benefit over Liu's detector.

D. Conditional Probability Detector of Chapple et al. [2]

This detector was also modified from that found in Chapple *et al.* [2]. A moving window (see Figure 4) forms an annulus around a centre pixel and the probability of seeing the centre pixel given the background annulus is calculated. The decision variable is given by

$$X^* C_X^{-1} X - Y^* C_Y^{-1} Y$$

where X is a column vector comprised of the data values in the annulus,

$$X = [S_{HH}^{(1)}, S_{HV}^{(1)}, S_{VV}^{(1)}, \ldots, S_{HH}^{(N)}, S_{HV}^{(N)}, S_{VV}^{(N)}]^T$$

and Y is X with the centre pixel data appended,

$$Y = [S_{HH}^{(0)}, S_{HV}^{(0)}, S_{VV}^{(0)}, X^T]^T.$$

Here C_X and C_Y are covariance matrices which as usual are estimated from the SAR ocean data only. The conditional probability detector showed a small improvement over Liu's detector.

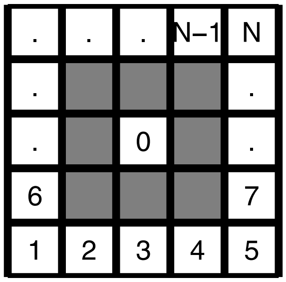

Fig. 4. The Conditional Probability Detector format. The guard area which prevents ship pixels corrupting the background ocean pixels is shaded in grey.

E. Pauli double bounce detector

The Pauli decomposition of a scattering matrix S uses the Pauli basis. Thus, assuming reciprocity so that $S_{HV} = S_{VH}$, S is represented as a weighted sum:

$$[S] = \begin{bmatrix} S_{HH} & S_{HV} \\ S_{HV} & S_{VV} \end{bmatrix} = \alpha[S]_a + \beta[S]_b + \gamma[S]_c$$

where the coefficients α, β and γ are given by

$$\alpha = (S_{HH} + S_{VV})/\sqrt{2} \quad (2)$$

$$\beta = (S_{HH} - S_{VV})/\sqrt{2} \quad (3)$$

$$\gamma = 2S_{HV}/\sqrt{2}. \quad (4)$$

These complex coefficients are interpreted as follows: α determines the amount of single or odd-bounce scatter in S, β determines the amount of double or even-bounce scatter, and γ determines the amount of scatter from dihedrals rotated by $45°$. Note that, there are many arrangements of scatterers which can produce the same scattering matrix and this interpretation of the Pauli coefficients does not necessarily represent the true situation. Since man-made targets are comprised of flat plates which are often roughly at right angles to one another, it is expected that they will generate a significant amount of double-bounce scatter. Thus large values of $|\beta|^2$ can indicate man-made targets. However, the absolute size of $|\beta|^2$ is related to the size of the target. In order to assess the pure polarimetric properties, it was decided to normalise $|\beta|^2$ by expressing it as a fraction of the total power. Thus

$$\frac{|\beta|^2}{|\alpha|^2 + |\beta|^2 + |\gamma|^2}$$

is used as the ship detection statistic.

V. Stripmap SAR detection results

The initial analysis consisted of comparing a variety of single polarisation channels. These provide a benchmark for assessing the improvement from detectors which use more than one polarisation channel. For the single polarisation channels, the detections are made by simply thresholding the measured backscatter value. The results are shown in Figure 5 and confirm known trends. In particular, the HV, LL and cross-slant 45 channels all perform well.

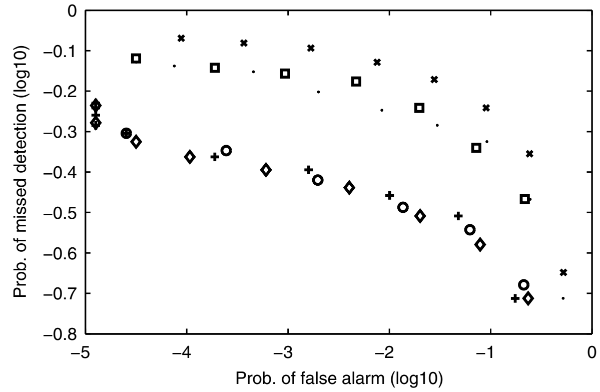

Fig. 5. Single polarisation channel ROC curves: ‘diamond’ is LL; ‘o’ is HV; ‘+’ is cross-slant 45; ‘.’ is HH; ‘square’ is SPAN; and ‘x’ is VV. Both axes are on a log10 scale. Lines closer to the bottom left hand corner have better detection performance.

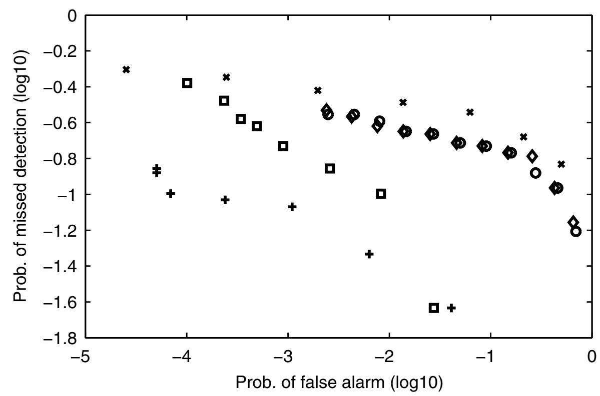

Fig. 6. Multi-polarisation channel ROC curves: ‘+’ is Significance Test Detector; ‘square’ is HH-VV correlation; ‘o’ is Liu’s Detector; ‘diamond’ is conditional probability detector; and ‘x’ is the HV channel for comparison. Both axes are on a log10 scale. Lines closer to the bottom left hand corner have better detection performance.

In Figure 6, the results for the other detectors of Section III are shown. The HV channel (which was the best of the single polarisations) and the HH-VV correlation coefficient are shown for comparison. These tests indicate that the Significance Test Detector is the preferred algorithm. Its improved performance over the Liu’s detector is due to the exploitation of spatial correlations. The conditional probability detector performs as well as Liu’s detector but will also improve if the central window is enlarged to exploit spatial correlations. It is of interest to note that the HH-VV correlation performs well only at high probabilities of false alarm – thus the Significance Test is making use of other features of the polarimetric data. Note also that the benefit of using spatial correlations will depend on the spatial resolution of the SAR imagery and the size and length of the ship’s being sought.

VI. Circular spotlight SAR detection results

A consideration to bare in mind when interpreting these results of this section is that the spatial correlations in the

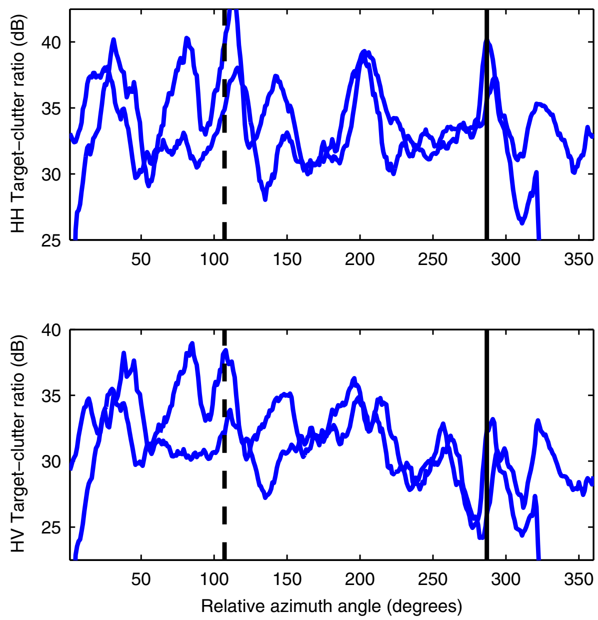

Fig. 7. Variation in the target-clutter ratio with azimuth angle for the circular spotlight imagery. Top - HH polarisation channel; bottom - HV. The solid (dashed) vertical line indicates the azimuth for which the radar is viewing the ship bow-on (stern-on). The two orbits have been overlaid and match well. The data have been smoothed with a box car filter of length 9.

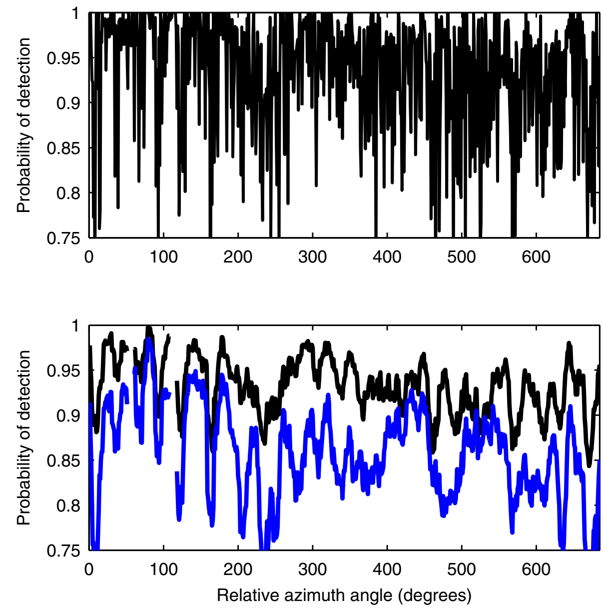

Fig. 8. Variation in probability of detection against azimuth angle at a fixed probability of false alarm of 10^{-5} for the Liu detector. Top - without smoothing. Bottom - after smoothing with a box car filter of length 9. The Liu detector is shown in black while the HV detector is shown in blue for comparison.

imagery have not been exploited. The decision not to make use of the spatial correlations was taken because the aim here is to assess the benefits of polarimetry. Thus while the ship is easy to detect visually, this is misleading since the eye takes account of the spatial correlations. Note too that the manual ground-truthing is not perfect and some ocean pixels may have been classified as ship pixels.

The variation in the ship-to-ocean backscatter ratio for the circular spotlight imagery is shown in Figure 7. For the HH polarisation plot there are six peaks. Four of these align with the cardinal ship directions (bow-on, broadside and stern-on). The remaining two peaks are located near the stern-on peak and a conjectured to be a multiple bounce interaction with the ocean, stern and trawl bars. While it can be seen that the ratio is high (typically greater than 30 dB), the performance of the detectors considered in this section is not as good as expected. The explanation is that the plotted ratio represents averaged values (and hence includes spatial correlations), while detection performance depends on the distribution of the backscatter values not just averages.

The performance of the Liu detector (and the HV detector for comparison) is shown in Figure 8. Owing to the limited number of ship pixels in each SAR image (of the order of 100 to 200), it is difficult to estimate useful ROC curves. Instead the probability of detection for a fixed probability of false alarm of 10^{-5} is plotted. The detection results are reasonably good with a probability of detection typically better than 0.9. Again it is clear that using multiple polarisation channels is better than only one.

One striking feature of the data is the noisiness of the results - see the top plot in Figure 8. There are two possible causes: variation in the backscatter response due to randomness in the ship backscatter; and poor estimates of the co-variance matrix (owing to the small number of samples used). The ocean is a complex and chaotic environment and so, as discussed below, the first is more likely. Future work will assess the accuracy of the co-variance matrix estimates.

It was expected that the detection performance would be correlated with the azimuth angle. This expectation was based on the obvious correlations in the ship-to-ocean backscatter ratio as shown in Figure 7. However the lack of trends is clear and the likely explanation is that backscatter distributions need to be taken in to account.

The output from the Pauli double bounce detector is shown in Figure 9. Note the significant increase in the double bounce component when the ship is viewed from one of cardinal orientations (bow-on, broadside or stern-on). This is to be expected since the ship construction is box-like and aligned with the ship heading. This comment also applies to any double bounce that arises from scattering off the ocean and on to the ship and visa-versa. At oblique angles, such double bounce scatter will not be returned to the radar. The detection performance for the Pauli double bounce detector is not particularly good with low probabilities of detection.

The Krogager polarimetric decomposition was also applied to the circular spotlight data with results no better than those for the Pauli double bounce detector. These poor results and the lack of clear trends in the Liu detector performance

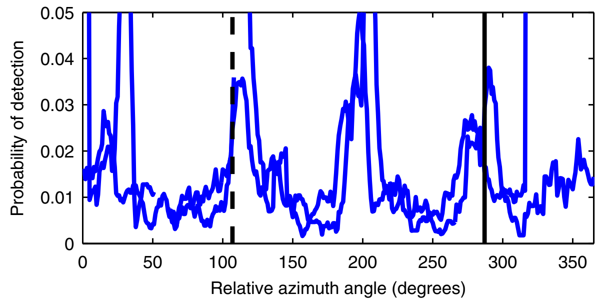

Fig. 9. Variation in probability of detection against azimuth angle at a fixed probability of false alarm of 10^{-5} for the Pauli detector. The two orbits have been overlaid and match well. The solid vertical line marks the azimuth for which the ship is heading toward the radar (i.e. viewed bow-on), and the dashed line corresponds to the ship heading away from the radar (i.e. viewed stern-on). A box car filter of length 9 was used to smooth the data.

against azimuth are contrary to results previously reported in the literature. However, in the case of maritime data, similar problems have been noted before [7]. Consequently, a brief investigation was undertaken using sub-apertures. The sub-aperture results agreed with Greidanus' findings [9], and showed that ship backscatter response changes from sub-aperture to sub-aperture. An example, of sub-aperture results for the imagery used here is shown in Figure 10. The sub-apertures were formed by splitting the azimuth

The variability from sub-aperture to sub-aperture is likely to be due to ship motion while the SAR is being collected. The effects of target motion on SAR imagery have been studied before [8]. Target motion causes azimuth shifting and smearing of the backscatter. The result is that the scatter from physically distinct scattering elements can be mixed together in complicated ways. Moreover, for a ship, the proportions of the mixture will be time varying as the ship pitches and rolls. Such variation is likely to corrupt the polarimetric properties of the backscatter. It is conjectured that the poor results presented here are due to ship motion effects and that they have been exacerbated by the small vessel size (and consequent more severe chaotic motion).

VII. Co-variance matrix variation with azimuth

The full Liu detector as described in Equation 1 makes use of the polarimetric co-variance matrix of both the ocean and the vessel. In order to better understand the performance of this detector it is useful to examine the elements of the covariance matrix. In particular, it would be useful to know how robust the covariance matrix is to changes of azimuth angle and to determine the range of azimuth angles over which a particular co-variance matrix estimate can be used. The work in this section is a preliminary investigation of these questions. The interpretation of some of the data plotted is ongoing and only a few general comments are made here.

It is also important to note here that the Pauli and Krogager detectors mentioned in the previous section are so called "coherent decompositions". Coherent decompositions assume the backscatter response is deterministic and repeatable. As

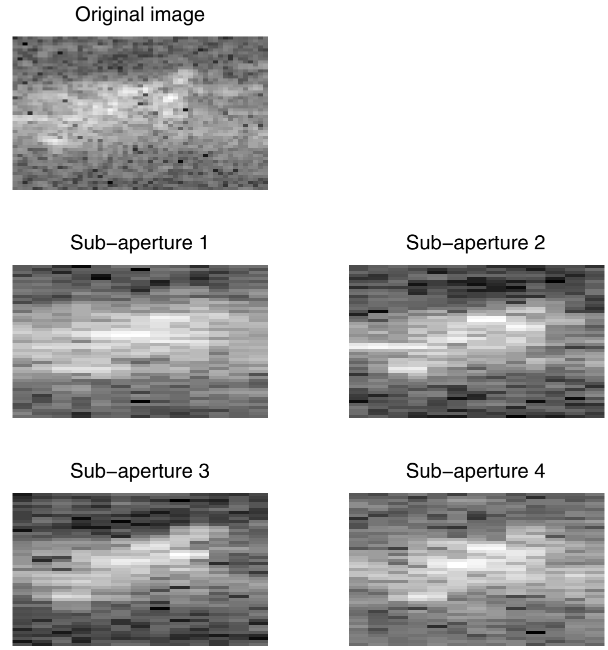

Fig. 10. Illustration of the effect of vessel motion while being imaged. The full resolution image is shown at the top. The sub-apertures were formed by splitting the azimuth bandwidth into 4 separate non-overlapping bands. The effect is to form reduced azimuth resolution images at different times during the SAR image formation process. The variability amongst the sub-aperture images is due to vessel motion while being imaged.

discussed in the last section that is unlikely to be the case for the maritime data considered here. The other type of decompositions are known as "incoherent decompositions". Incoherent decompositions assume the backscatter is random and hence use averaging to estimate the underlying physical scattering parameters. Such considerations apply to the covariance matrix too.

Under the assumption of reciprocity (i.e. $S_{HV} = S_{VH}$) the elements of the co-variance matrices are estimated by

$$C_{ij} = E[S_i S_j{}^*] \tag{5}$$

where $i, j = 1, 2, 3$ and S_1, S_2, S_3 denote S_{HH}, S_{HV}, S_{VV} and $E(\cdot)$ is the expectation operator and $*$ denotes the complex conjugate operator. The co-variance matrix is, by definition, Hermitian and so the diagonal elements are real and there are only three independent off-diagonal elements. It can be shown that the diagonal elements satisfy

$$\sigma^0_{HH} = 4\pi C_{11} \quad \sigma^0_{HV} = 4\pi C_{22} \quad \sigma^0_{VV} = 4\pi C_{33}$$

where σ^0_{HH}, σ^0_{HV} and σ^0_{VV} are the usual backscatter coefficients. In place of the off-diagonal elements, it is more usual to use the complex correlation coefficients. They are normalised versions of the off-diagonal elements and are defined by

$$\rho_{ij} = \frac{C_{ij}}{\sqrt{C_{ii}C_{jj}}} = \frac{E[S_i S_j{}^*]}{\sqrt{E[|S_{ii}|^2]E[|S_{jj}|^2]}} = |\rho_{ij}|e^{i\theta}.$$

In the following we present the variation with azimuth of the three backscatter coefficients, the three correlation coefficient

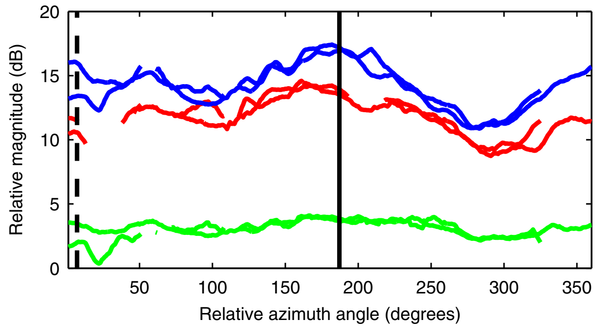

Fig. 11. Variation in backscatter coefficient magnitudes against azimuth angle for the ocean. Red - HH; green - HV; blue VV. The upwind azimuth is marked by a solid vertical line and downwind a dashed line.

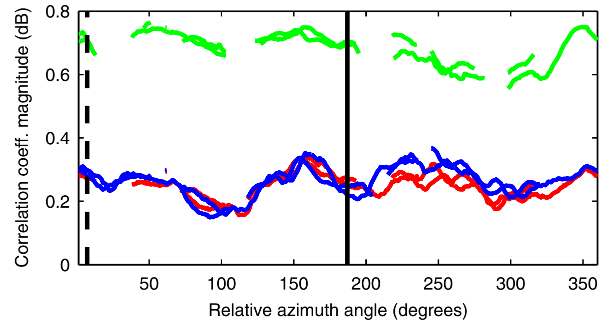

Fig. 13. Variation in the correlation coefficient magnitudes against azimuth angle for the ocean. Red - $|\rho_{HHHV}|$; green - $|\rho_{HHVV}|$; blue $|\rho_{HVVV}|$. Wind directions are as for Figure 11

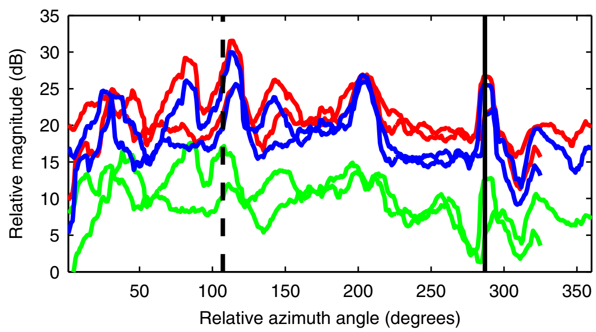

Fig. 12. Variation in backscatter coefficient magnitudes against azimuth angle for the ship. Red - HH; green - HV; blue VV. The bow-on azimuth is marked by a solid vertical line and the stern-on a dashed line.

magnitudes and the three correlation coefficient phases for the ocean. Lee *et al.* have derived the statistical distributions of these quantities under the assumption of a multi-variate complex Gaussian distribution [10]. Yueh *et al.* have established special properties under the assumption of a reflection symmetric scattering target [11]. They also present some measured data and theoretical models for ocean backscatter data.

The backscatter coefficient magnitudes for the ocean and ship are shown in Figures 11 and 12. These plots, like the others below have been edited to remove bad data points caused by saturation of the ADCs in the radar receiver. The ocean results are as expected and conform to know trends [4]. Note though that the cross wind trough at azimuth angle $290°$ is significantly deeper that at $100°$. This may reflect complex nature of the wave field with more than just wind driven waves present, but it is also possible that the aircraft orbit was not perfect and that the incidence angle varied.

The ship results are also readily interpreted with peaks in the four cardinal ship directions (bow-on, broadside and stern-on) as discussed above for the ship-to-ocean backscatter ratio plots. The two peaks located near the stern-on peak are again present. (As before, they are conjectured to be a multiple bounce interaction with the ocean, stern and trawl bars.)

The plots indicate that the HH/VV polarisation ratio maybe useful for ship detection since the ratio is above one for the ship and below one for the ocean, but care needs to be taken here. These plots represent averaged quantities and, for individual pixel ratios, the distribution of the backscatter measurements will have an effect. In hard ship detection problems the number of available ship pixels will be small and covariance matrix estimates difficult.

The next plot, Figure 13, shows the correlation coefficient magnitudes for the ocean. The curves exhibit some of the properties discussed by Yueh *et al.* in [11] but there are also differences. Yueh *et al.* give a theoretical proof that in the case of reflection symmetric media $|\rho_{HHHV}|$ and $|\rho_{HVVV}|$ will be zero when measured in the azimuthal directions corresponding to the symmetries. In ideal conditions, the ocean surface has reflection symmetry for azimuthal directions corresponding to upwind, downwind and crosswind. While the plotted data have dips at these directions they do not decrease to zero. Yueh *et al.* also present the predictions of an earlier sea surface scattering model. The shape of the predictions for $|\rho_{HHHV}|$ and $|\rho_{HVVV}|$ are similar to the data presented in Figure 13. Similarly, $|\rho_{HHVV}|$ has qualitatively the expected behaviour with high values at all azimuths but it remains near 0.7 rather than 1.0.

Finally, Figure 14 shows the correlation coefficient phases for the ocean. Again, the data is qualitatively similar to the predictions of Yueh *et al.*. But as before, a full analysis of these features has not yet been done and only a few initial comments are made here. The theoretical model of Yueh *et al.* predicts the phase angle $\arg(\rho_{HHVV})$ to be zero. Clearly, the measured data is in close agreement with this prediction. However, the theoretical model also predicts both $\arg(\rho_{HHHV})$ and $\arg(\rho_{HVVV})$ to alternate between zero and $\pm\pi$ with no intermediary values which is not the case for the data here.

In future work it is intended to further analyse and interpret the results of this section and to investigate the consequences for ship detection algorithms. We note however, that any difference in polarimetric covariance matrix statistics which can be exploited for target detection purposes, is already built into the Liu detector and so improved performance on that

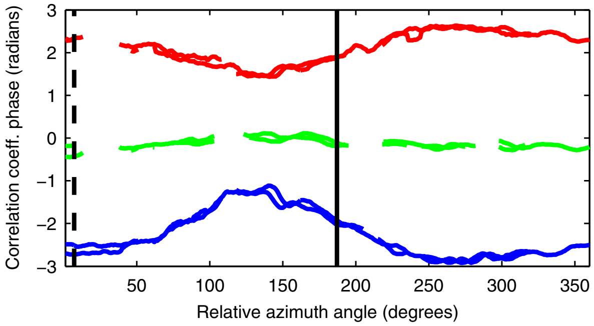

Fig. 14. Variation in the correlation coefficient phases against azimuth angle for the ocean. Red - $\arg(\rho_{HHHV})$; green - $\arg(\rho_{HHVV})$; blue $\arg(\rho_{HVVV})$. Wind directions are as for Figure 11

basis alone is not to be expected.

VIII. Conclusion

The study here is preliminary only and more work needs to be done. The stripmap results indicate that of the single polarisation channels, HV, LL and cross-slant $45°$ all provide good performance. Note that the incidence angle of the stripmap imagery was $40°$, and that at angles larger than $40°$ HH is also known to perform well. The stripmap results also show the significant performance improvement when multiple polarisation channels are used and spatial correlations are taken into account. ROC curves have been presented which quantify this improvement.

The circular spotlight imagery results showed that detection performance is variable with respect to azimuth angle and trends are hard to discern. Moreover, the performance of purely polarimetric detectors (i.e. detectors which are invariant under changes of backscatter magnitude) is generally poor. It is conjectured that, for the circular spotlight imagery, ship pitching motion degrades the polarimteric backscatter response making it more random than would otherwise be the case.

It is clear from the results of the last section that the elements of ocean polarimetric co-variance matrix are sensitive to changes of azimuth angle. While the elements change relatively slowly, the cumulative effect is significant. It follows that, a range of co-variance matrix estimates are needed if the ship detectors based on them are to be effective in all conditions. Using the plots as a guide, it is recommended that co-variance matrices be re-estimated at least every $30°$. Future work address this question more rigorously using detection performance measures.

IX. Acknowledgements

The RADARSAT-2 imagery used in this paper were collected as part of the Science and Operational Applications Research for RADARSAT-2 Program (SOAR).

References

[1] C. Liu, P.W. Vachon and G.W. Geling, “Improved ship detection with airborne polarimetric SAR data”, Canadian Journal of Remote Sensing, Vol 31, No 1, pp 122–131, 2005.

[2] P.B. Chapple, D.C. Bertilone, R.S. Caprari and G.N. Newsam, “Stochastic Model-Based Processing for Detection of Small Targets in Non-Gaussian Natural Imagery”, IEEE Trans. Image Proc., Vol 10, No 4, pp 554–564, 2001.

[3] N.J.S. Stacy, D.P. Badger, A.S. Goh, M. Preiss, and M.L. Williams, “The DSTO Ingara airborne X-Band SAR polarimetric upgrade: first results”, IEEE 2003 International Geoscience and Remote Sensing Symposium (IGARSS'03), Vol 7, pp 4474–6, 2003.

[4] Crisp, D.J.; Stacy, N.J.S.; Hudson, D.A.; Pincus, P.B.; Goh, A.S. “Polarimetric analysis of maritime SAR data collected with the DSTO Ingara X-Band radar” IEEE 2007 International Geoscience and Remote Sensing Symposium (IGARSS'07) pp 3870–3873, 2007.

[5] Touzi, R. “On the use of polarimetric SAR data for ship detection” IEEE 1999 International Geoscience and Remote Sensing Symposium (IGARSS '99) Vol 2, pp 812–814, 1999.

[6] Dong, Y. “High grazing angle and high resolution sea clutter: correlation and polarisation analyses” Defence Science & Technology Organisation, Technical Report DSTO-TR-1972, Mar 2007.

[7] Margarit, G., Mallorqui, J. J. and Rius J. M. “On the Usage of GRECOSAR, an Orbital Polarimetric SAR Simulator of Complex Targets, to Vessel Classification Studies” IEEE Trans. Geoscience and Remote Sensing, Vol 44, No 12, pp 3517–3526, Dec 2006.

[8] Raney, K. “Synthetic aperture imaging and moving targets.” IEEE Trans. on Aerospace and Electronic Systems, AES-7, Vol 3, pp 498–505, May 1971

[9] Greidanus, H. “Sub-aperture Behavior of SAR Signatures of Ships” IEEE 2006 International Geoscience and Remote Sensing Symposium (IGARSS 2006) pp 3579–3582, 2006.

[10] Lee, Jong-Sen; Hoppel, K. W.; Mango, S. A.; Miller, A. R. “Intensity and phase statistics of multilook polarimetric and interferometric SAR imagery” IEEE Transactions on Geoscience and Remote Sensing, Vol 32, No 5, pp. 1017–1028, 1994.

[11] Yueh, S. H., R. Kwok and S. V. Nghiem “Polarimetric scattering and emission properties of targets with reflection symmetry” Radio Science, 29(6), 1409–1420, 1994.